

Rate constants from the reaction path Hamiltonian. II. Nonseparable semiclassical transition state theory

Baron Peters and Alexis T. Bell

Department of Chemical Engineering, University of California, Berkeley, California 94720

Arup Chakraborty^{a)}

Department of Chemical Engineering, University of California, Berkeley, California 94720;

Department of Chemistry, University of California, Berkeley, California 94720;

Materials Sciences Division, Lawrence Berkeley National Laboratory, University of California, Berkeley, California 94720; and Physical Biosciences Division, Lawrence Berkeley National Laboratory, University of California, Berkeley, California 94720

(Received 19 April 2004; accepted 9 June 2004)

For proton transfer reactions, the tunneling contributions to the rates are often much larger than thermally activated rates at temperatures of interest. A number of separable tunneling corrections have been proposed that capture the dependence of tunneling rates on barrier height and imaginary frequency size. However, the effects of reaction pathway curvature and barrier anharmonicity are more difficult to quantify. The nonseparable semiclassical transition state theory (TST) of Hernandez and Miller [Chem. Phys. Lett. **214**, 129 (1993)] accounts for curvature and barrier anharmonicity, but it requires prohibitively expensive cubic and quartic derivatives of the potential energy surface at the transition state. This paper shows how the reaction path Hamiltonian can be used to approximate the cubic and quartic derivatives used in nonseparable semiclassical transition state theory. This enables tunneling corrections that include curvature and barrier anharmonicity effects with just three frequency calculations as required by a conventional harmonic transition state theory calculation. The tunneling correction developed here is nonseparable, but can be expressed as a thermal average to enable efficient Monte Carlo calculations. For the proton exchange reaction $\text{NH}_2 + \text{CH}_4 \rightleftharpoons \text{NH}_3 + \text{CH}_3$, the nonseparable rates are very accurate at temperatures from 300 K up to about 1000 K where the TST rate itself begins to diverge from the experimental results. © 2004 American Institute of Physics. [DOI: 10.1063/1.1778162]

I. INTRODUCTION

The availability of fast electronic structure algorithms is making it possible to carry out calculations of accurate reaction rate constants.¹ However, some factors in rate constant calculations remain difficult to quantify. Paper I (Ref. 2) showed how the reaction path Hamiltonian³ (RPH) can be constructed and used to generate a correction for the effects of barrier recrossing. This paper shows how a small portion of the RPH near the transition state can be used to compute an accurate, nonseparable, semiclassical tunneling correction⁴ that accounts for barrier anharmonicity and reaction pathway curvature.

Several tunneling corrections have been developed.⁵ Simple tunneling models include the parabolic barrier,^{6,7} the truncated parabolic barrier,⁸ the small curvature tunneling model,^{9–13} and interpolated Eckart-barrier models.^{11,12,14,15} More computationally demanding models include fully anharmonic nonseparable semiclassical transition state theory (SCTST),⁴ semiclassical initial value representation methods,^{16–19} and instanton models that rigorously sum over all tunneling paths.¹⁵ Sophisticated tunneling models often require a detailed description of the potential energy surface.

For example, fully anharmonic SCTST requires cubic and quartic derivatives of the potential energy at the transition state.^{4,20} Because *ab initio* cubic and quartic potential energy derivatives must be obtained by finite difference methods, anharmonic SCTST becomes prohibitively expensive for reactions with as few as ten atoms.

The method developed here requires the reactant and transition state energies and frequencies and a small portion of the minimum energy path²¹ (MEP) near the transition state. The RPH curvature coupling elements³ and the potential energy profile from the small portion of the MEP (Ref. 3) can be used to obtain anharmonic constants for nonseparable, anharmonic SCTST. Like the truncated parabolic barrier,⁸ the SCTST developed here includes a maximum barrier penetration integral to ensure proper temperature dependence at low temperatures. A general limitation of nonseparable SCTST is that an explicit sum over states is required, which converges slowly at high temperatures. The sum over states in this paper has been expressed as a thermal average to enable efficient Monte Carlo calculations.²² For brevity, this method is referred to as RPH-SCTST throughout this work.

The first section of this paper reviews the parabolic barrier SCTST, truncated parabolic barrier SCTST, and fully anharmonic SCTST to motivate RPH-SCTST. The second section develops RPH-SCTST from the reaction path Hamiltonian. The final section applies RPH-SCTST to the hydro-

^{a)}Author to whom correspondence should be addressed. Electronic mail: arup@uclink.berkeley.edu

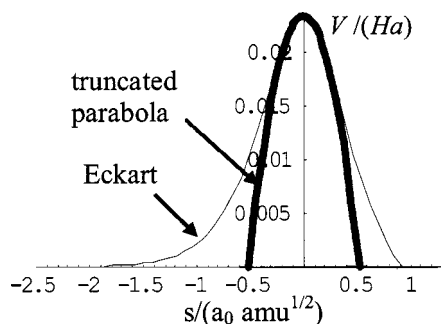


FIG. 1. Truncated parabolic barrier for the $\text{NH}_2 + \text{CH}_4$ reaction, shown with the more realistic asymmetric Eckart barrier (Refs. 9 and 12).

gen abstraction reaction $\text{NH}_2 + \text{CH}_4 \rightleftharpoons \text{NH}_3 + \text{CH}_3$, and compares the results with those obtained from other semiclassical tunneling theories and experiments.^{23–25}

II. REVIEW OF SEMICLASSICAL TRANSITION STATE THEORIES

Semiclassical transition state theories are often based on WKB tunneling probabilities. The probability of transmission through a one-dimensional barrier is $\{1 + \exp[2\theta(E)]\}^{-1}$, where E is the energy of the incoming packet. The potential energy profile $V(s)$ determines the barrier penetration integral $\theta(E)$ through the equation

$$\theta(E) = \frac{1}{\hbar} \int_{s_1(E)}^{s_2(E)} ds \sqrt{2\mu[V(s) - E]}, \quad (1)$$

where s is a distance reaction coordinate, μ is the reduced mass associated with the packet ($\mu=1$ in mass weighted coordinates), $V(s)$ is the one-dimensional barrier energy, and $s_1(E)$ and $s_2(E)$ are the classical turning points that mark the beginning and end of the classically forbidden region, $V(s_1(E)) = V(s_2(E)) = E$. The WKB transmission probability can be used directly in one-dimensional models, or generalized to multidimensional systems through instanton models or perturbation theories.

A commonly used tunneling correction describes the barrier as an infinite, one-dimensional parabola having an imaginary frequency at the saddle point of magnitude ω_F .^{6,7} With $\beta = (kT)^{-1}$ the correction is

$$\Gamma_{\text{Harm.}} = \frac{\beta \hbar \omega_F / 2}{\sin(\beta \hbar \omega_F / 2)}. \quad (2)$$

The harmonic result breaks down for $kT_c \leq \hbar \omega_F / 2\pi$.⁷ The breakdown at temperatures below T_c occurs because the Boltzmann distribution, $\exp(-E/kT)$, grows to infinity faster than the temperature independent decay of the barrier penetration probability. The divergence can be removed by reintroducing an energetic minimum, or equivalently, a maximum barrier penetration integral.

Auerbach and Fermann have developed a separable SCTST for a truncated parabolic barrier⁸ having the imaginary frequency of the saddle point. Figure 1 shows a truncated parabolic barrier and the corresponding asymmetric

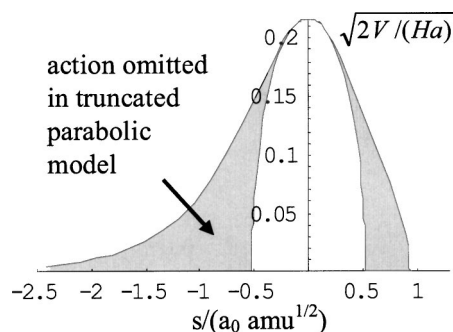


FIG. 2. Nearly half of the barrier penetration integral for the Eckart barrier is omitted by the truncated parabolic barrier model at the ground state energy.

Eckart barrier.¹¹ The specific barrier parameters have been chosen to fit the zero point energy and imaginary frequency of the barrier for the $\text{NH}_2 + \text{CH}_4$ reaction.

The tunneling correction for the truncated parabolic barrier is⁸

$$\Gamma_{\text{Auerb.}} = \frac{1}{2} \left[e^{\beta V_{\text{ZP}} - \theta_0} \text{sech } \theta_0 + \int_{-\infty}^{\theta_0} d\theta e^{\beta V_{\text{ZP}} \theta / \theta_0} \text{sech}^2 \theta \right], \quad (3)$$

where V_{ZP} is the difference between the zero point energy at the saddle point and the reactant minimum, i.e., the energetic reaction threshold. For the truncated harmonic barrier the maximum barrier penetration integral is given by

$$\theta_0 = \frac{\pi V_{\text{ZP}}}{\hbar \omega_F}. \quad (4)$$

$\Gamma_{\text{Auerb.}}$ is well behaved at all temperatures, and it has been shown that the slope of $\Gamma_{\text{Auerb.}}$ versus $1/T$ is correct in both the high and low temperature limits.⁸ However, $\Gamma_{\text{Auerb.}}$ ignores the effects of reaction path curvature and barrier anharmonicity. The truncated parabolic barrier approach tends to exaggerate tunneling rates because the square root dependence in the barrier penetration integral accentuates the tails of the potential energy profile that extend beyond the truncated parabolic barrier. The omitted portion of the barrier penetration integrand (for tunneling from the ground state energy) is shown as the shaded area in Fig. 2.

Miller and Hernandez have developed an anharmonic, nonseparable SCTST that includes cornercutting, barrier anharmonicity, and other factors.⁴ Their rate constant is given by

$$k(T) = \frac{k_B T}{2\hbar Z_R} \int_{-\infty}^{\infty} d\theta \text{sech}^2 \theta \sum_{n^\ddagger} \exp[-\beta E(n^\ddagger, \theta)], \quad (5)$$

where

$$E(n^\ddagger, \theta) = V_{n^\ddagger} - \hbar \varpi_{n^\ddagger} \frac{\theta}{\pi} - \hbar \chi_{FF} \frac{\theta^2}{\pi^2}, \quad (6)$$

$$V_{n^\ddagger} = V_{\text{ZP}} + \sum_{k=1}^{F-1} \hbar \omega_k n_k + \sum_{k' \leq k}^{F-1} \hbar \chi_{k'k} \left(n_k + \frac{1}{2} \right) \left(n_{k'} + \frac{1}{2} \right), \quad (7)$$

$$\varpi_{n^\ddagger} = \omega_F + i \sum_{k=1}^{F-1} \chi_{kF} \left(n_k + \frac{1}{2} \right). \quad (8)$$

The first $F-1$ angular frequencies are the transverse frequencies in the RPH at the saddle point. The last frequency ω_F is the magnitude of the imaginary frequency at the saddle point. The normal modes establish a rectilinear coordinate system $(\mathbf{Q}, Q_F) = (Q_1, \dots, Q_{F-1}, Q_F)$ in which each Q_k represents the displacement from the saddle point along the corresponding eigenvector.^{4,20} The spectroscopic constants, χ_{lm} , are defined in terms of the saddle point frequencies, the full set of cubic derivatives and a subset of the quartic derivatives of the potential with respect to the coordinates (\mathbf{Q}, Q_F) at the saddle point.²⁰ The spectroscopic constants at the transition state perturbatively account for the effects of reaction path curvature, barrier anharmonicity, rovibrational coupling, and transverse mode anharmonicity. Complete expressions for the spectroscopic constants at the transition state are given in a separate paper by Hernandez and Miller.²⁰

The reaction coordinate anharmonicity, χ_{FF} , is usually negative²⁰ which ensures a finite rate constant at all temperatures, even without an imposed maximum barrier penetration integral. Equation (5) does allow tunneling from below the reaction threshold which may result in incorrect low temperature behavior. Anharmonic SCTST could be improved by enforcing a maximum possible barrier penetration integral, and developing a feasible scheme for computing the spectroscopic constants in Eqs. (6)–(8).

III. SCTST FROM THE REACTION PATH HAMILTONIAN

RPH-SCTST uses the RPH curvature coupling elements at the saddle point, $\mathbf{b}(0)$, and the potential energy along the MEP near the saddle point, $V_0(s)$.³ The RPH coordinates, (\mathbf{q}, s) , are identical to the (\mathbf{Q}, Q_F) coordinate system of anharmonic SCTST at the saddle point.²⁶ For points away from the saddle point, $(\mathbf{q}, s) = (\mathbf{Q}, Q_F) = \mathbf{0}$, the coordinate systems diverge due to path curvature and twisting of the transverse modes. The equation linking the coordinate systems is

$$\tilde{\mathbf{L}} \begin{bmatrix} \mathbf{Q} \\ Q_F \end{bmatrix} = [\mathbf{a}(s) - \mathbf{a}(0)] + \mathbf{L}(s)\mathbf{q}, \quad (9)$$

where the matrix of F vectors, $[\mathbf{L}(s), \mathbf{a}'(s)]$, is comprised of transverse eigenvectors of the projected Hessian, $\mathbf{L}_1(s), \dots, \mathbf{L}_{F-1}(s)$, and the path tangent at an arclength s along the MEP as prescribed by the reaction path Hamiltonian. $\tilde{\mathbf{L}}$ is the eigenvector matrix at the saddle point, $[\mathbf{L}(0), \mathbf{a}'(0)]$. Taylor expanding the right side of Eq. (9) in s around $s=0$, and introducing the identity as $\tilde{\mathbf{L}}\tilde{\mathbf{L}}^T$, gives

$$\begin{aligned} \tilde{\mathbf{L}} \begin{bmatrix} \mathbf{Q} \\ Q_F \end{bmatrix} &= \mathbf{L}(0)\mathbf{q} + \mathbf{a}'(0)s + \frac{s^2}{2}\tilde{\mathbf{L}}\tilde{\mathbf{L}}^T\mathbf{a}''(0) + \dots \\ &+ s\tilde{\mathbf{L}}\tilde{\mathbf{L}}^T\mathbf{L}'(0)\mathbf{q} + \dots \\ &\approx \tilde{\mathbf{L}} \left(1 + s \begin{bmatrix} \mathbf{B} & \mathbf{b}/2 \\ -\mathbf{b} & 0 \end{bmatrix} \right) \begin{bmatrix} \mathbf{q} \\ s \end{bmatrix}. \end{aligned} \quad (10)$$

In the last approximation the RPH coupling constants at the saddle point are abbreviated as $\mathbf{b}=\mathbf{b}(0)$ and $\mathbf{B}=\mathbf{B}(0)$. When $\mathbf{B}=\mathbf{0}$, the change of variables becomes

$$\begin{aligned} Q_F &= s(1 - \mathbf{q} \cdot \mathbf{b}), \\ Q_k &= q_k + \frac{s^2}{2}b_k, \end{aligned} \quad (11)$$

where $k \neq F$. A treatment of the more general case with non-zero Coriolis coupling is outlined in the Appendix. The Coriolis couplings \mathbf{B} result in transitions among the transverse modes, but are not expected to be as important for tunneling as the curvature couplings \mathbf{b} . Equation (11) can be inverted locally to obtain

$$\begin{aligned} q_k &= Q_k - \frac{1}{2}s^2b_k, \\ s &= (\mathbf{b} \cdot \mathbf{b})^{-1/3} \left(\left[Q_F + \left(\frac{8(1 - \mathbf{Q} \cdot \mathbf{b})^3}{27\mathbf{b} \cdot \mathbf{b}} + Q_F^2 \right)^{1/2} \right]^{1/3} \right. \\ &\quad \left. + \left[Q_F - \left(\frac{8(1 - \mathbf{Q} \cdot \mathbf{b})^3}{27\mathbf{b} \cdot \mathbf{b}} + Q_F^2 \right)^{1/2} \right]^{1/3} \right). \end{aligned} \quad (12)$$

From Eq. (12), the cubic and quartic force constants can be evaluated as functions of RPH parameters. The force constants given here reflect the assumption of constant transverse frequencies near the saddle point, $d\Omega^2(s)/ds = \mathbf{0}$. The resulting cubic and necessary quartic derivatives with respect to the (\mathbf{Q}, Q_F) variables are

$$\begin{aligned} f_{kFF} &= -\frac{2}{3}b_k(\omega_F^2 + 3\omega_k^2), \\ f_{FFF} &= V_0'''(0), \\ f_{kkFF} &= -\frac{2}{9}b_k^2(5\omega_F^2 + 12\omega_k^2), \end{aligned} \quad (13)$$

$$f_{FFFF} = V_0''''(0) + 12b^2\omega_F^2 + 6 \sum_{k=1}^{F-1} b_k^2\omega_k^2,$$

$$f_{kkk} = f_{kk1} = f_{klm} = f_{kkF} = f_{klF} = f_{kkkk} = f_{kkll} = 0.$$

Here a subscript $k \neq F$ on f indicates a derivative of the potential with respect to the transverse coordinate Q_k at the saddle point, and a subscript F indicates a derivative with respect to Q_F , the reaction coordinate, at the saddle point. Many of the derivatives are zero because the Coriolis couplings in \mathbf{B} were assumed to be zero. These derivatives can then be used to calculate the spectroscopic constants²⁰ for anharmonic SCTST.

$$\begin{aligned} \chi_{kk} &= \chi_{k'k} = 0, \\ \chi_{FF} &= \frac{-\hbar}{16\omega_F^2} \left(f_{FFFF} + \frac{5f_{FFF}^2}{3\omega_F^2} - \sum_{k=1}^{F-1} \frac{f_{kFF}^2(8\omega_F^2 + 3\omega_k^2)}{\omega_k^2(4\omega_F^2 + \omega_k^2)} \right), \end{aligned} \quad (14)$$

$$i\chi_{kF} = \frac{\hbar}{\omega_k\omega_F} \left(f_{kkFF} + \frac{2f_{kFF}^2}{\omega_k^2 + 4\omega_F^2} \right).$$

The rovibrational terms²⁰ have been neglected for this hydrogen exchange reaction because they contribute less than 3 cm^{-1} to the anharmonic constants. Rather than use the anharmonic constants directly in Eq. (5), we integrate only to the reaction threshold energy as done for the truncated parabolic barrier. This is equivalent to defining the state-dependent maximum barrier penetration integral so that the energy equals the reactant energy in state \mathbf{n} , or equivalently

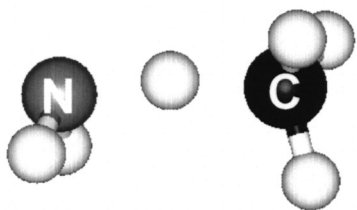


FIG. 3. Saddle point geometry at CCSD(T)/6-311++G** level. The central proton is 1.27 Å from the nitrogen nucleus and 1.31 Å from the carbon nucleus. The angle formed by these atoms is 169.8°.

$$V_{\text{zp}} + \sum_{k=1}^{F-1} \hbar \delta \omega_k n_k - \frac{\theta_0}{\pi} \left(\hbar \tilde{\omega}_F + i \sum_{k=1}^{F-1} \hbar \chi_{kF} n_k \right) - \hbar \chi_{FF} \frac{\theta_0^2}{\pi^2} = 0, \quad (15)$$

where $\delta \omega_k$ is the difference between the k th frequency at the saddle point and the k th frequency in the reactant basin, and $\tilde{\omega}_F = \omega_F + (i \sum_{k=1}^{F-1} \hbar \chi_{kF} / 2)$.

With these definitions, the RPH-SCTST rate constant becomes $k_{\text{RPH-SCTST}} = k_{\text{TST}} \Gamma_{\text{RPH-SCTST}}$, where

$$\Gamma_{\text{RPH-SCTST}} = \frac{1}{2} \left\langle \exp \left[\beta \hbar \sum_{k=1}^{F-1} \delta \omega_k n_k + \beta V_{\text{zp}} - \theta_0 \right] \text{sech } \theta_0 \right\rangle + \frac{1}{2} \left\langle \int_{-\infty}^{\theta_0} d\theta \exp \left[\beta \hbar \tilde{\omega}_F \frac{\theta}{\pi} + \beta \hbar \chi_{FF} \frac{\theta^2}{\pi^2} + \beta \hbar i \frac{\theta}{\pi} \sum_{k=1}^{F-1} \chi_{kF} n_k \right] \text{sech}^2 \theta \right\rangle. \quad (16)$$

The thermal averages are taken with respect to the Hamiltonian, $\hbar \sum_k \omega_k n_k$. Because the entire MEP is not computed, the $F-1$ largest frequencies ordered from largest to smallest at the minimum are assumed to correspond to the real frequencies at the transition state. For a bimolecular reactant, the last five frequencies are zero, forcing an explicit sum over the corresponding degrees of freedom.

IV. EXAMPLE: $\text{NH}_2 + \text{CH}_4 \rightleftharpoons \text{CH}_3 + \text{NH}_3$

The proton exchange reaction between CH_4 and NH_2 is a good test reaction for several reasons. Accurate experimental data are available over a wide range of temperatures extending well below the limit of harmonic SCTST.^{23–25} The reaction is a prototypical high curvature, “heavy-light-heavy” reaction²⁶ where a light proton is transferred between relatively bulky NH_2 and CH_3 groups. The imaginary frequency at the transition state is nearly $2000(i) \text{ cm}^{-1}$, so the parabolic barrier is narrow compared to the anharmonic barrier. Finally, the electronic structures of all involved species are sufficiently simple to allow *ab initio* calculations of high quality and accuracy.

The reactants (NH_2 and CH_4), products (NH_3 and CH_3), and the transition state (shown in Fig. 3) were optimized at the CCSD(T)/6-311++G** level. Absolute energies of all stationary points were taken from these calculations.

TABLE I. Energy relative to reactants in kcal/mol. Zero point corrections are not included. The QCISD(T)/6-311+G(2df,2p) results are from Yu *et al.* (Ref. 28).

	‡	Products
CCSD(T)/6-311++G**	15.39	−1.74
QCISD(T)/6-311+G(2df/2p)	14.93	−2.26
Experimental estimate	15.16±0.8	−1.14

To obtain the curvature and barrier anharmonicity, 13 points were computed along the steepest descent path at the CCSD(T)/6-311G** level.²⁷ The points included the saddle point, $s=0$, and six points in each channel at distances of $s=0.008, 0.016, 0.032, 0.064, 0.096$, and $0.128 (a_0 \text{ amu}^{1/2})$ along the steepest descent path from the saddle point. A starting Hessian with one imaginary frequency was obtained at the B3LYP/6-311G** level to initiate the steepest descent path. The SR1 formula²⁸ was used to update the Hessian at each point to approximately follow the quadratic steepest descent path.²⁹ Values of ω_F^2 , f_{sss} , and f_{ssss} , were obtained from a best fit quartic polynomial of the CCSD(T)/6-311G** energies along this portion of the steepest descent path. The saddle point was reoptimized at the B3LYP/6-311++G** level to obtain transverse frequencies for use in the rate calculations. Frequencies of reactants and products were also computed for re-optimized structures at the B3LYP/6-311++G** level. Table I shows the classical and zero point energies of the transition state and the products with respect to the reactant energies.

Table II shows the saddle point frequencies, the curvature coupling components, the spectroscopic constants χ_{kF} and the $\delta \omega$ frequencies of Eqs. (15) and (16). The curvature coupling elements have units of $(a_0^{-1} \text{ amu}^{-1/2})$. The computed frequencies at the transition state are similar to values reported by Yu *et al.*³⁰ except for the smallest transverse frequency of 148 cm^{-1} . The corresponding frequency obtained

TABLE II. Transition state frequencies, RPH curvature coupling elements, spectroscopic constants, and difference between transition state and reactant frequencies. The table also shows the imaginary frequency and the barrier anharmonicity, χ_{FF} .

k	$\omega_k (\text{cm}^{-1})$	$b_k (\text{a.u.})$	$i\chi_{kF} (\text{cm}^{-1})$	$\delta \omega_k (\text{cm}^{-1})$
1	3495.7	−0.009	0.01	45.6
2	3398.3	0.034	0.07	41.3
3	3189.6	0.007	0.00	55.0
4	3181.1	−0.002	0.00	48.0
5	3057.5	0.031	0.04	−70.4
6	1562.3	0.005	0.00	−1462.7
7	1484.3	0.007	0.00	−74.0
8	1442.3	0.017	−0.01	−115.0
9	1416.3	0.011	−0.01	−92.8
10	1335.0	0.158	−1.29	−8.5
11	1164.9	0.089	−0.46	−175.6
12	853.1	−0.061	−0.27	−483.2
13	781.2	−0.004	0.00	781.2
14	560.2	0.347	−12.27	560.2
15	391.4	−0.013	−0.02	391.4
16	370.0	−0.078	−0.90	370.0
17	147.8	−0.014	−0.21	147.8
F	1973.5(i)		−267.19(i)	

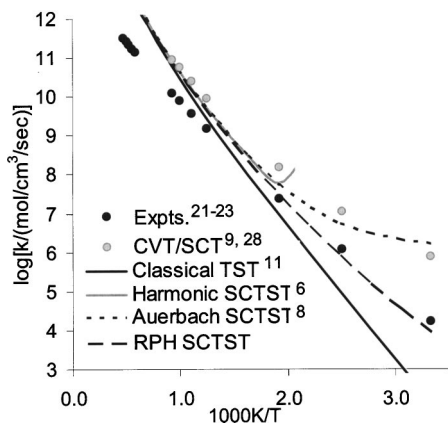


FIG. 4. Arrhenius plot showing the rate constants from various theoretical methods (Refs. 6, 8, 9, and 11) and experimental measurements (Refs. 21–23). The CVT/SCT transmission coefficient obtained by Yu *et al.* (Ref. 28) was multiplied by the TST rate from this work to generate a CVT/SCT rate for comparison.

by Yu *et al.* at the QCISD(T)/6-311G** level was only 50 cm^{-1} . The frequencies of Yu *et al.* result in rate constants that are only slightly different than the rates reported here.

The rate constants that result from a number of semiclassical transition state theories are shown in Fig. 4. The SCTST rates all approach the classical TST rate in the high temperature limit. Note that classical harmonic TST performs poorly at temperatures above 1000 K. As a result, all of the SCTST rates overestimate the rate by nearly two orders of magnitude at 2000 K. A possible explanation is that the harmonic models of the transition state and the reactants are inadequate at high temperatures where vibrationally excited energy levels become heavily populated. Barrier recrossing could also lower the rate constant at high temperatures. This possibility was investigated using the reactive flux simulation method described in Paper I. The dynamic corrections were small, ranging from 0.7 at 2000 K to 0.9 at 666.7 K using a B3LYP/6-311++G** reaction path Hamiltonian. Recrossing is not sufficient to account for the discrepancy between predicted and measured rates at high temperatures. We note, however, that the reactive flux simulation method used here cannot capture recrossing for tunneling trajectories. Simultaneous description of dynamic recrossing and nonseparable tunneling requires a more rigorous treatment such as a path integral calculation of the flux-flux correlation function.

At low temperatures, the various SCTST rates behave very differently. Harmonic SCTST breaks down at 454 K, 154° above the lowest temperature experimental data of Demissy and Leclaux.²³ The SCTST rate of Auerbach and Fermann can be computed at all temperatures. However, Auerbach's SCTST overestimates the true rate at all temperatures. The Arrhenius plot for Auerbach's SCTST rate also has far more upward curvature than the experimental data. The RPH-SCTST rates match the experimental data very well for temperatures between 300 and 500 K. Additionally, the Arrhenius plot for the RPH-SCTST rate appears to have curvature similar to the low temperature experimental data.

For comparison, the small curvature tunneling correction obtained by Yu *et al.*³⁰ has also been applied to our classical

TST rate. The CVT/SCT correction results in an overestimate of the rate at low temperatures and an excessively curved Arrhenius plot, much like Auerbach's SCTST. Note that the SCT correction was calculated using a slightly smaller barrier of 14.93 kcal/mol and a slightly larger imaginary frequency of $2121(i) \text{ cm}^{-1}$ as compared to this study. Nevertheless, RPH-SCTST most accurately describes the temperature dependence of the hydrogen abstraction rate.

V. CONCLUSIONS

The semiclassical rate theory presented here, RPH-SCTST, is qualitatively correct in the low and high temperature limits. The new correction captures the effects of curvature and barrier anharmonicity with just three frequency calculations as required by a standard harmonic TST calculation. The results of this paper show that the effect of barrier anharmonicity can result in calculated rates that are much smaller than rates predicted by truncated harmonic SCTST. Comparison to experimental data for the hydrogen abstraction reaction $\text{NH}_2 + \text{CH}_4 \rightleftharpoons \text{NH}_3 + \text{CH}_3$ suggests that RPH-SCTST is quantitatively reliable at low temperatures. Finally, the nonseparable correction has been written in the form of a thermal average to enable the use of efficient Monte Carlo sampling techniques for computation.

ACKNOWLEDGMENTS

The authors are grateful for useful discussions with Professor W. H. Miller and Professor Attila Szabo. The authors are also grateful to Professor Martin Head-Gordon who provided Q-Chem 2.1 (Ref. 31) for this work. The authors would like to thank Professor Wan-Zhen Liang for valuable assistance with Q-Chem. The authors acknowledge British Petroleum for support. One of the authors (B.P.) acknowledges NSF for fellowship support.

APPENDIX: FORCE CONSTANTS WITH CORIOLIS COUPLING

The RPH potential is easily differentiated with respect to the (\mathbf{q}, s) variables, and Eq. (10) can be differentiated to obtain derivatives of the (\mathbf{q}, s) coordinates with respect to the (\mathbf{Q}, Q_F) coordinates. Thus a straightforward application of the chain rule gives the following expression for the cubic force constants:

$$\frac{\partial^3 V}{\partial Q_i \partial Q_j \partial Q_k} = \frac{\partial^3 V}{\partial q_m \partial q_n \partial q_p} \frac{\partial q_m}{\partial Q_i} \frac{\partial q_n}{\partial Q_j} \frac{\partial q_p}{\partial Q_k} + \frac{\partial V}{\partial q_m} \times \frac{\partial^3 q_m}{\partial Q_i \partial Q_j \partial Q_k} + \frac{\partial^2 V}{\partial q_m \partial q_n} \left(\frac{\partial q_m}{\partial Q_i} \frac{\partial^2 q_n}{\partial Q_j \partial Q_k} + \frac{\partial q_m}{\partial Q_j} \frac{\partial^2 q_n}{\partial Q_i \partial Q_k} + \frac{\partial q_m}{\partial Q_k} \frac{\partial^2 q_n}{\partial Q_i \partial Q_j} \right). \quad (\text{A1})$$

Here we have used Einstein notation and defined $q_F = s$. The same approach applies to the quadratic force constants.

The force constants in Eq. (13) followed from the assumption of zero Coriolis coupling, $\mathbf{B}=\mathbf{0}$. By repeated differentiation of Eq. (10) we can obtain force constants that include Coriolis effects. For notational convenience, we make the following definitions:

$$\mathbf{M} = \begin{bmatrix} \mathbf{B} & \mathbf{b}/2 \\ -\mathbf{b} & 0 \end{bmatrix}, \quad \Delta = \begin{bmatrix} \frac{\partial q_l}{\partial Q_l} & \dots & \frac{\partial q_l}{\partial Q_F} \\ \vdots & & \vdots \\ \frac{\partial s}{\partial Q_l} & \dots & \frac{\partial s}{\partial Q_F} \end{bmatrix}, \quad (\text{A2})$$

$$\Delta_F = \begin{bmatrix} \frac{\partial s}{\partial Q_l} & \dots & \frac{\partial s}{\partial Q_F} \end{bmatrix}, \quad \mathbf{e}_k = \begin{bmatrix} \delta_{kl} \\ \vdots \\ \delta_{kF} \end{bmatrix}.$$

Differentiating Eq. (10) with respect to (\mathbf{Q}, Q_F) gives the equations

$$\mathbf{I} = (\mathbf{I} + s\mathbf{M})\Delta + \mathbf{M} \begin{bmatrix} \mathbf{q} \\ s \end{bmatrix} \circ \Delta_F. \quad (\text{A3})$$

These are trivially solved to give the first derivatives as $\Delta = \mathbf{I}$ at the saddle point, $(\mathbf{q}, s) = \mathbf{0}$. A second differentiation gives

$$\frac{\partial \Delta}{\partial Q_k} = -\mathbf{M}(\delta_{kF} + \mathbf{e}_k \circ \mathbf{e}_F^T) \quad (\text{A4})$$

at the saddle point. The third derivatives at the saddle point are given by

$$\begin{aligned} \frac{\partial^2 \Delta}{\partial Q_k \partial Q_{k'}} &= -\mathbf{M} \left[\frac{\partial^2 s}{\partial Q_k \partial Q_{k'}} + \delta_{kF} \frac{\partial \Delta}{\partial Q_{k'}} + \delta_{k'F} \frac{\partial \Delta}{\partial Q_k} \right. \\ &\quad + \left(\frac{\partial^2}{\partial Q_k \partial Q_{k'}} \begin{bmatrix} \mathbf{q} \\ s \end{bmatrix} \right) \circ \mathbf{e}_F^T + \mathbf{e}_{k'} \circ \left(\frac{\partial \Delta_F}{\partial Q_k} \right) \\ &\quad \left. + \mathbf{e}_k \circ \left(\frac{\partial \Delta_F}{\partial Q_{k'}} \right) \right]. \quad (\text{A5}) \end{aligned}$$

Note that in the force constant expressions [e.g., Eq. (A1)] the highest derivative of (\mathbf{q}, s) with respect to (\mathbf{Q}, Q_F) is multiplied by a first derivative of the potential energy at the saddle point. Thus evaluation of the cubic force constants

only requires first and second derivatives of (\mathbf{q}, s) . Similarly, evaluation of the quartic force constants only requires first, second, and third derivatives of (\mathbf{q}, s) .

- ¹T. Helgaker, P. Jorgensen, and J. Olsen, *Molecular Electronic Structure Theory* (Wiley, Sussex, England, 2000).
- ²B. G. Peters, A. T. Bell, and A. K. Chakraborty, *J. Chem. Phys.* **121**, 4453 (2004), preceding paper.
- ³W. H. Miller, N. C. Handy, and J. E. Adams, *J. Chem. Phys.* **72**, 99 (1980).
- ⁴R. Hernandez and W. H. Miller, *Chem. Phys. Lett.* **214**, 129 (1993).
- ⁵V. A. Benderskii, V. I. Goldanskii, and D. E. Makarov, *Phys. Rep.* **233**, 195 (1993).
- ⁶E. Wigner, *Z. Phys. Chem. Abt. B* **19**, 203 (1932).
- ⁷R. P. Bell, *Trans. Faraday Soc.* **55**, 1 (1959).
- ⁸J. T. Fermann and S. Auerbach, *J. Chem. Phys.* **112**, 6787 (2000).
- ⁹W. H. Miller, *J. Chem. Phys.* **53**, 3578 (1970).
- ¹⁰R. A. Marcus and M. E. Coltrin, *J. Chem. Phys.* **67**, 2609 (1977).
- ¹¹A. Gonzalez-Lafont, T. N. Truong, and D. G. Truhlar, *J. Chem. Phys.* **95**, 8875 (1991).
- ¹²Y.-Y. Chuang and D. G. Truhlar, *J. Phys. Chem. A* **101**, 3808 (1997).
- ¹³D. G. Truhlar, B. C. Garrett, and S. J. Klippenstein, *J. Phys. Chem.* **100**, 12771 (1996).
- ¹⁴W. T. Duncan, R. L. Bell, and T. N. Truong, *J. Comput. Chem.* **19**, 1039 (1998).
- ¹⁵W. H. Miller, Y. Zhao, M. Ceotto, and S. Yang, *J. Chem. Phys.* **119**, 1329 (2003).
- ¹⁶H. Wang, X. Sun, and W. H. Miller, *J. Chem. Phys.* **108**, 9726 (1998).
- ¹⁷X. Sun and W. H. Miller, *J. Chem. Phys.* **110**, 6635 (1999).
- ¹⁸H. Wang, M. Thoss, and W. H. Miller, *J. Chem. Phys.* **112**, 47 (2000).
- ¹⁹A. Fernandez-Ramos, D. G. Truhlar, J. C. Corchado, and J. Espinosa-Garcia, *J. Phys. Chem. A* **106**, 4957 (2002).
- ²⁰R. Hernandez, W. H. Miller, N. C. Handy, D. Jayatilaka, and A. Willetts, *Chem. Phys. Lett.* **172**, 62 (1990).
- ²¹H. B. Schlegel, *J. Comput. Chem.* **24**, 1514 (2003).
- ²²D. Chandler, *Introduction to Modern Statistical Mechanics* (Oxford University Press, New York, 1987).
- ²³M. Demissy and R. Lesclaux, *J. Am. Chem. Soc.* **102**, 2897 (1980).
- ²⁴W. Hack, H. Kurzke, P. Roveirolles, and H. G. Wagner, *Ber. Bunsenges. Phys. Chem.* **90**, 1210 (1986).
- ²⁵G. Henning and H. G. Wagner, *Ber. Bunsenges. Phys. Chem.* **99**, 863 (1995).
- ²⁶R. T. Skodje, *Annu. Rev. Phys. Chem.* **44**, 145 (1993).
- ²⁷M. Page and J. W. McIver, *J. Chem. Phys.* **88**, 922 (1988).
- ²⁸J. Nocedal and S. J. Wright, *Numerical Optimization* (Springer, New York, 1999).
- ²⁹J.-Q. Sun and K. Ruedenberg, *J. Chem. Phys.* **99**, 5269 (1993).
- ³⁰Y.-X. Yu, S.-M. Li, Z.-F. Xu, Z.-S. Li, and C.-C. Sun, *Chem. Phys. Lett.* **296**, 131 (1998).
- ³¹J. Kong *et al.*, *J. Comput. Chem.* **21**, 1532 (2000).